

Shape evolution of giant resonances in Nd and Sm isotopes

Kenichi Yoshida^{1,2} and Takashi Nakatsukasa²

¹ *Department of Physics, Graduate School of Science and Technology, Niigata University, Niigata 950-2181, Japan*

² *RIKEN Nishina Center for Accelerator-Based Science, Wako, Saitama 351-0198, Japan*

(Dated: September 17, 2021)

Giant multipole resonances in Nd and Sm isotopes are studied by employing the quasiparticle-random-phase approximation on the basis of the Skyrme energy-density-functional method. Deformation effects on giant resonances are investigated in these isotopes which manifest a typical nuclear shape change from spherical to prolate shapes. The peak energy, the broadening, and the deformation splitting of the isoscalar giant monopole (ISGMR) and quadrupole (ISGQR) resonances agree well with measurements. The magnitude of the peak splitting and the fraction of the energy-weighted strength in the lower peak of the ISGMR reflect the nuclear deformation. The experimental data on ISGMR, ISGDR, and ISGQR are consistent with the nuclear-matter incompressibility $K \simeq 210 - 230$ MeV and the effective mass $m_0^*/m \simeq 0.8 - 0.9$. However, the high-energy octupole resonance (HEOR) in ^{144}Sm seems to indicate a smaller effective mass, $m_0^*/m \simeq 0.7 - 0.8$. A further precise measurement of HEOR is desired to determine the effective mass.

PACS numbers: 21.10.Re; 21.60.Jz; 24.30.Cz

I. INTRODUCTION

Giant resonance (GR) is a typical high-frequency collective mode of excitation in nuclei [1]. Effects of the nuclear deformation on the GRs have been investigated both experimentally and theoretically. Among them, the deformation splitting of the isovector giant dipole resonance (GDR), due to different frequencies of oscillations along the major- and minor-axis [2], is well established. A textbook example of the evolution of the GDR as a function of the mass number can be found in Refs. [3, 4]. Emergence of a double-peak structure of the photoabsorption cross section of ^{150}Nd and ^{152}Sm clearly indicates an onset of the deformation in the ground state. For the GRs with higher multipolarity, although the deformation splitting is less pronounced, the peak broadening has been observed [1]. The detailed and systematic investigations on the GRs would give us a unique information on the shape phase transition in nuclei.

In contrast to low-energy modes of excitation in nuclei, the GRs substantially reflect bulk nuclear properties. Thus, their studies may provide information on the nuclear matter. The GRs can be qualitatively investigated by using various macroscopic models, such as fluidynamical models which properly take account of deformation of the Fermi sphere [5]. However, a quantitative description of the GRs requires a microscopic treatment of nuclear response. For heavy deformed open-shell nuclei, the leading theory for this purpose is, currently, the quasiparticle-random-phase approximation (QRPA) based on the nuclear energy-density-functional (EDF) method [6]. The QRPA based on the deformed ground-state configuration with superfluidity is able to treat a variety of excitations in the linear regime. A role of deformation on GRs has been studied by means of the deformed QRPA employing the Gogny interaction in the light mass region [7]. GRs in heavy systems have been investigated using Skyrme functionals, where the separa-

ble approximation is employed for the residual interaction [8], and using the relativistic EDF [9].

The Hartree-Fock-Bogoliubov (HFB) mean field formulated in the two-dimensional cylindrical coordinates and the deformed QRPA in the quasiparticle basis have been developed recently [10]. The application, however, was restricted to light systems [11] because of the large computer memory demanded for storing the matrix elements, and the time-consuming calculation for diagonalizing a non-symmetric matrix of several tens or hundreds of thousands of dimensions. The deformed Skyrme-QRPA calculation utilizing the transformed harmonic oscillator basis is also restricted to light nuclei due to the same stumbling block [12]. Recently, the finite amplitude method [13, 14] is applied to the harmonic-oscillator-basis deformed QRPA and the calculation for heavy systems becomes possible with an inexpensive numerical cost [15], while it is restricted to the $K^\pi = 0^+$ mode so far.

In this article, we develop a new calculation code of the deformed HFB and QRPA for use in the massively parallel computers to examine the applicability of the Skyrme-EDF-based QRPA to the excitation modes in heavy deformed systems. Using this new parallelized code, the deformation effects on the GRs in Nd and Sm isotopes will be discussed. A part of the results has already appeared in Ref. [16], where we demonstrated that the deformed QRPA can describe well the broadening and the deformation splitting of the isovector GDR in nuclei undergoing the shape phase transition. In the present paper, we perform numerical analysis for the GRs of multipolarity $L = 0 - 3$ with both isoscalar (IS) and isovector (IV) characters, and examine the incompressibility and the effective mass both in spherical and deformed nuclei. It should be noted that, in Ref. [17], the deformation splitting of the giant monopole resonance (GMR) in neutron-rich Zr isotopes is predicted by utilizing the calculation code in this article.

The article is organized as follows: In Sec. II, the deformed Skyrme-EDF-QRPA method is recapitulated. In Sec. II B, some technical details to reduce the computational cost are given. In Sec. III, results of the numerical analysis of the GRs in the Nd and Sm isotopes with shape changes are presented. Finally, the summary is given in Sec. IV.

II. DEFORMED HFB + QRPA

A. Basic equations

The axially deformed HFB in the cylindrical-coordinate space with the Skyrme EDF and the QRPA in the quasiparticle (qp) representation can be found in Ref. [10]. Here, we briefly describe the outline of the formulation.

To describe the nuclear deformation and the pairing correlations, simultaneously, in good account of the continuum, we solve the HFB equations [18, 19]

$$\begin{pmatrix} h^q(\mathbf{r}\sigma) - \lambda^q & \tilde{h}^q(\mathbf{r}\sigma) \\ \tilde{h}^q(\mathbf{r}\sigma) & -(h^q(\mathbf{r}\sigma) - \lambda^q) \end{pmatrix} \begin{pmatrix} \varphi_{1,\alpha}^q(\mathbf{r}\sigma) \\ \varphi_{2,\alpha}^q(\mathbf{r}\sigma) \end{pmatrix} = E_\alpha \begin{pmatrix} \varphi_{1,\alpha}^q(\mathbf{r}\sigma) \\ \varphi_{2,\alpha}^q(\mathbf{r}\sigma) \end{pmatrix} \quad (1)$$

in real space using cylindrical coordinates $\mathbf{r} = (\rho, z, \phi)$. Here, $q = \nu$ (neutron) or π (proton). We assume axial and reflection symmetries. Since we consider the even-even nuclei only, the time-reversal symmetry is also assumed. A nucleon creation operator $\hat{\psi}^\dagger(\mathbf{r}\sigma)$ at the position \mathbf{r} with the intrinsic spin σ is written in terms of the qp wave functions as

$$\hat{\psi}^\dagger(\mathbf{r}\sigma) = \sum_\alpha \varphi_{1,\alpha}(\mathbf{r}\bar{\sigma}) \hat{\beta}_\alpha^\dagger + \varphi_{2,\alpha}^*(\mathbf{r}\sigma) \hat{\beta}_\alpha. \quad (2)$$

The notation $\varphi(\mathbf{r}\bar{\sigma})$ is defined by $\varphi(\mathbf{r}\bar{\sigma}) = -2\sigma\varphi(\mathbf{r} - \sigma)$.

For the mean-field Hamiltonian h , we mainly employ the SkM* functional [20]. For the pairing energy, we adopt the one in Ref. [21] that depends on both the isoscalar (ϱ) and the isovector (ϱ_1) densities, in addition to the pairing density ($\tilde{\varrho}$):

$$\mathcal{H}_{\text{pair}}(\mathbf{r}) = \frac{V_0}{4} \sum_q g_q[\varrho, \varrho_1] [\tilde{\varrho}(\mathbf{r})]^2, \quad (3)$$

with

$$g_q[\varrho, \varrho_1] = 1 - \eta_0 \frac{\varrho(\mathbf{r})}{\varrho_0} - \eta_1 \frac{\tau_3 \varrho_1(\mathbf{r})}{\varrho_0} - \eta_2 \left[\frac{\varrho_1(\mathbf{r})}{\varrho_0} \right]^2. \quad (4)$$

Here $\varrho_0 = 0.16 \text{ fm}^{-3}$ is the saturation density of symmetric nuclear matter, with the parameters (η_0, η_1 and η_2) given in Table III of Ref. [21]. Because of the assumption of the axially symmetric potential, the z -component of the qp angular momentum, Ω , is a good quantum number. Assuming time-reversal symmetry and reflection

symmetry with respect to the $x - y$ plane, the space for the calculation can be reduced into the one with positive Ω and positive z only.

Using the qp basis obtained as a self-consistent solution of the HFB equations (1), we solve the QRPA equation in the matrix formulation [22]

$$\sum_{\gamma\delta} \begin{pmatrix} A_{\alpha\beta\gamma\delta} & B_{\alpha\beta\gamma\delta} \\ -B_{\alpha\beta\gamma\delta} & -A_{\alpha\beta\gamma\delta} \end{pmatrix} \begin{pmatrix} X_{\gamma\delta}^i \\ Y_{\gamma\delta}^i \end{pmatrix} = \hbar\omega_i \begin{pmatrix} X_{\alpha\beta}^i \\ Y_{\alpha\beta}^i \end{pmatrix}. \quad (5)$$

The residual interaction in the particle-hole (p-h) channel appearing in the QRPA matrices A and B is derived from the Skyrme EDF. The residual Coulomb interaction is neglected because of the computational limitation. We expect that the residual Coulomb plays only a minor role [23–26]. In Ref. [24], effects of neglecting the residual Coulomb interaction are discussed in details: The centroid energy of the GDR can be shifted by about 400 keV at maximum. However, this amount of change does not affect the discussion in the present paper. We also drop the so-called “ J^2 ” term C_t^T both in the HFB and QRPA calculations. The residual interaction in the particle-particle (p-p) channel is derived from the pairing EDF (3). It is noted here that we have an additional contribution to the residual interaction in the p-h channel coming from the pairing EDF (3) because of the squared η_2 term in Eq. (3) (see Appendix A).

B. Details of the numerical calculation

For solution of the HFB equations (1), we use a lattice mesh size $\Delta\rho = \Delta z = 0.6 \text{ fm}$ and a box boundary condition at $\rho_{\text{max}} = 14.7 \text{ fm}$, $z_{\text{max}} = 14.4 \text{ fm}$. The differential operators are represented by use of the 11-point formula of finite difference method. Since the parity (π) and the magnetic quantum number (Ω) are good quantum numbers, the HFB Hamiltonian becomes in a block diagonal form with respect to each (Ω^π, q) sector. The HFB equations for each sector are solved independently with 48 processors for the qp states up to $\Omega = 23/2$ with positive and negative parities. Then, the densities and the HFB Hamiltonian are updated, which requires communication among the 48 processors. The modified Broyden’s method [27] is utilized to calculate new densities. The qp states are truncated according to the qp energy cutoff at $E_\alpha \leq 60 \text{ MeV}$.

We introduce the additional truncation for the QRPA calculation, in terms of the two-quasiparticle (2qp) energy as $E_\alpha + E_\beta \leq 60 \text{ MeV}$. This reduces the number of 2qp states to, for instance, about 38 000 for the $K^\pi = 0^-$ excitation in ^{154}Sm . The calculation of the QRPA matrix elements in the qp basis is performed in the parallel computers. In the present calculation, all the matrix elements are real and we use 512 processors to compute them. The two-dimensional block cyclic distribution is employed to keep a good load balancing.

To save the computing time for diagonalization of the QRPA matrix, we employ a technique to reduce the non-Hermitian eigenvalue problem to a real symmetric matrix of half the dimension [5, 28]. For diagonalization of the matrix, we use the ScaLAPACK PDSYEV subroutine [29]. To calculate the QRPA matrix elements and to diagonalize the matrix, it takes about 390 CPU hours and 135 CPU hours, respectively on the RICC, the supercomputer facility at RIKEN.

The similar calculations of the HFB+QRPA for axially deformed nuclei have been recently reported [7, 9, 12, 30]. Among them, the one by Terasaki and Engel in Ref. [30] is analogous to ours. They adopt the canonical-basis representation and introduce a further truncation according to the occupation probabilities of 2qp excitations. In contrast, we adopt the qp representation and truncation simply due to the 2qp energies. However, we have a drawback in the computing time. Carrying out the numerical integration for the p-h matrix elements in the qp basis takes 4 times as long as the calculation in the canonical basis. For reference, we show the matrix elements of the QRPA in the qp basis in Appendix A.

Since the full self-consistency between the static mean-field calculation and the dynamical calculation is slightly violated by neglecting two-body Coulomb interaction and truncating the 2qp space, the spurious states may have finite excitation energies. In the present calculation, the spurious states for the $K^\pi = 0^+, 1^+, 0^-$ and 1^- excitations appear at 0.35 MeV, 0.34 MeV, $1.46i$ MeV and $1.60i$ MeV, respectively in ^{154}Sm . We see in section III.B the contamination of the spurious component in GRs to be small because the GRs are well apart from the spurious states in energy.

The transition strength distribution as a function of the excitation energy E is calculated as

$$S_\lambda^\tau(E) = \sum_i \sum_K \frac{\gamma/2}{\pi} \frac{|\langle i | \hat{F}_{\lambda K}^\tau | 0 \rangle|^2}{(E - \hbar\omega_i)^2 + \gamma^2/4}. \quad (6)$$

The smearing width γ is set to 2 MeV, which is supposed to simulate the spreading effect, Γ^\downarrow , missing in the QRPA. It is noted that in Ref. [16] we showed that the constant smearing parameter of $\gamma = 2$ MeV reproduces well the total width of the GDR in the Nd and Sm isotopes with $N = 82 - 92$.

Here we define the operators as

$$\hat{F}_{\lambda=0}^{\tau=0} = \sum_{\tau_3=1,-1} \int d\mathbf{r} r^2 \hat{\psi}_{\tau_3}^\dagger(\mathbf{r}) \hat{\psi}_{\tau_3}(\mathbf{r}), \quad (7)$$

$$\hat{F}_{\lambda=0}^{\tau=1} = \sum_{\tau_3=1,-1} \int d\mathbf{r} \tau_3 r^2 \hat{\psi}_{\tau_3}^\dagger(\mathbf{r}) \hat{\psi}_{\tau_3}(\mathbf{r}), \quad (8)$$

$$\hat{F}_{\lambda=1,K}^{\tau=0} = \sum_{\tau_3=1,-1} \int d\mathbf{r} r^3 Y_{1K}(\hat{r}) \hat{\psi}_{\tau_3}^\dagger(\mathbf{r}) \hat{\psi}_{\tau_3}(\mathbf{r}), \quad (9)$$

$$\hat{F}_{\lambda=1,K}^{\tau=1} = \int d\mathbf{r} r Y_{1K}(\hat{r}) \left\{ \frac{Z}{A} \hat{\psi}_\nu^\dagger(\mathbf{r}) \hat{\psi}_\nu(\mathbf{r}) - \frac{N}{A} \hat{\psi}_\pi^\dagger(\mathbf{r}) \hat{\psi}_\pi(\mathbf{r}) \right\}, \quad (10)$$

$$\hat{F}_{\lambda=2,K}^{\tau=0} = \sum_{\tau_3=1,-1} \int d\mathbf{r} r^2 Y_{2K}(\hat{r}) \hat{\psi}_{\tau_3}^\dagger(\mathbf{r}) \hat{\psi}_{\tau_3}(\mathbf{r}), \quad (11)$$

$$\hat{F}_{\lambda=2,K}^{\tau=1} = \sum_{\tau_3=1,-1} \int d\mathbf{r} \tau_3 r^2 Y_{2K}(\hat{r}) \hat{\psi}_{\tau_3}^\dagger(\mathbf{r}) \hat{\psi}_{\tau_3}(\mathbf{r}), \quad (12)$$

$$\hat{F}_{\lambda=3,K}^{\tau=0} = \sum_{\tau_3=1,-1} \int d\mathbf{r} r^3 Y_{3K}(\hat{r}) \hat{\psi}_{\tau_3}^\dagger(\mathbf{r}) \hat{\psi}_{\tau_3}(\mathbf{r}), \quad (13)$$

$$\hat{F}_{\lambda=3,K}^{\tau=1} = \sum_{\tau_3=1,-1} \int d\mathbf{r} \tau_3 r^3 Y_{3K}(\hat{r}) \hat{\psi}_{\tau_3}^\dagger(\mathbf{r}) \hat{\psi}_{\tau_3}(\mathbf{r}). \quad (14)$$

The spin index is omitted for simplicity in the above definition because the spin direction is unchanged by these operators.

III. RESULTS AND DISCUSSION

A. Ground state properties

We summarize in Table I the calculated ground-state properties of the Nd and Sm isotopes. Around $N = 82$, the systems are calculated to be spherical. The calculated quadrupole moment of $^{142,144}\text{Nd}$ and $^{144,146}\text{Sm}$ are very small but finite. This is due to the numerical error originating from the finite mesh size and breaking of the spherical symmetry of the rectangular box employed. Increase in the neutron number, the deformation gradually develops. As shown in Fig. 1 of Ref. [16], the calculation well reproduces the evolution of quadrupole deformation for $N \geq 86$.

The pairing gap disappears at $N = 82$ associated with the spherical magic number of neutrons. The obtained pairing gaps are in good agreement with the empirical values for deformed nuclei, while they are overestimated in the spherical systems. This is consistent with the findings of Ref. [31] that the pairing gaps of deformed nuclei are underestimated if we use the pairing functional adjusted to the experimental data for spherical nuclei. Note that the pairing functional employed in the present calculation is constructed by adjusting to the experimental pairing gaps of deformed nuclei [21].

B. Mixing of spurious center-of-mass motion

The isoscalar (IS) dipole operator, Eq. (9) contains the component of the center-of-mass motion. For deformed nuclei, the $K^\pi = 0^-$ and 1^- octupole operators may also excite the spurious center-of-mass motion. To examine the mixing of the spurious modes, we use the corrected operator;

$$\hat{F}_{\lambda=1,K}^{\tau=0} = \sum_{\tau_3} \int d\mathbf{r} (r^3 - \eta_{KR}) Y_{1K}(\hat{r}) \hat{\psi}_{\tau_3}^\dagger(\mathbf{r}) \hat{\psi}_{\tau_3}(\mathbf{r}) \quad (15)$$

instead of using Eq. (9). Here, the correction factor in the isoscalar dipole operator originally discussed for a spherical system (η) to subtract the spurious component of the

TABLE I. Ground state properties of Nd and Sm isotopes obtained by the deformed HFB calculation with the SkM* and pairing EDFs. Chemical potentials λ_q , deformation parameters β_2^q , quadrupole moments $\langle Q_2 \rangle_q$, average pairing gaps $\langle \Delta \rangle_q$, and root-mean-square radii $\sqrt{\langle r^2 \rangle_q}$ for neutrons and protons are listed.

	¹⁴² Nd	¹⁴⁴ Nd	¹⁴⁶ Nd	¹⁴⁸ Nd	¹⁵⁰ Nd	¹⁵² Nd	¹⁴⁴ Sm	¹⁴⁶ Sm	¹⁴⁸ Sm	¹⁵⁰ Sm	¹⁵² Sm	¹⁵⁴ Sm
λ_ν (MeV)	-8.79	-6.42	-6.65	-6.73	-7.03	-6.69	-9.12	-6.99	-7.21	-7.42	-7.58	-7.25
λ_π (MeV)	-5.23	-5.83	-6.25	-6.90	-7.72	-8.46	-4.39	-4.99	-5.37	-5.99	-6.60	-7.13
β_2^ν	0.00	0.00	0.12	0.18	0.26	0.30	0.00	0.00	0.12	0.20	0.27	0.30
β_2^π	0.00	0.00	0.14	0.21	0.30	0.34	0.00	0.00	0.14	0.22	0.30	0.33
$\langle Q_2 \rangle_\nu$ (fm ²)	~ 0	~ 0	328	530	796	939	~ 0	~ 0	323	563	805	939
$\langle Q_2 \rangle_\pi$ (fm ²)	~ 0	~ 0	251	389	568	644	~ 0	~ 0	257	435	597	668
$\langle \Delta \rangle_\nu$ (MeV)	0.00	0.82	0.93	1.06	0.99	0.78	0.00	0.86	0.98	1.10	1.07	0.90
$\langle \Delta \rangle_\pi$ (MeV)	1.71	1.67	1.48	1.30	0.87	0.54	1.75	1.72	1.57	1.35	1.04	0.90
$\sqrt{\langle r^2 \rangle_\nu}$ (fm)	4.95	4.99	5.03	5.08	5.15	5.20	4.97	5.00	5.04	5.10	5.16	5.20
$\sqrt{\langle r^2 \rangle_\pi}$ (fm)	4.86	4.87	4.90	4.93	4.99	5.02	4.89	4.90	4.93	4.98	5.02	5.06

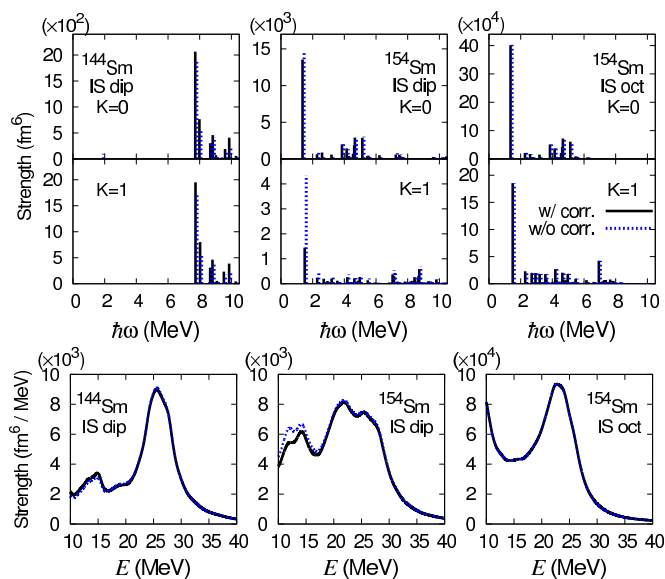


FIG. 1. (Color online) The IS dipole and octupole transition-strength distributions in ¹⁴⁴Sm and in ¹⁵⁴Sm in the low-energy region (upper panels) and the GR energy region (lower). The results obtained with $\eta_K = 0$ and $\eta_K^{(3)} = 0$ are shown by dotted lines.

center-of-mass motion [32] was extended to a deformed system (η_K) [10], and coincides with $\eta_K = \eta = 5/3$ in the spherical limit. For the octupole operators, we use a similar technique to the case of the dipole operator [33];

$$\hat{F}_{\lambda=3,K}^{\tau=0} = \sum_{\tau_3} \int dr [r^3 Y_{3K}(\hat{r}) - \eta_K^{(3)} r Y_{1K}(\hat{r})] \hat{\psi}_{\tau_3}^\dagger(\mathbf{r}) \hat{\psi}_{\tau_3}(\mathbf{r}). \quad (16)$$

It is noted that the correction factor $\eta_K^{(3)}$ vanishes in the spherical limit.

In Fig. 1 we show the IS dipole and octupole transition-strength distributions in the low-energy region in ¹⁴⁴Sm and ¹⁵⁴Sm, calculated with and without the correction

terms, η_K and $\eta_K^{(3)}$. In ¹⁴⁴Sm, because the transition strengths calculated with finite η_K are approximately identical to those with $\eta_K = 0$, the low-energy dipole states around 8 MeV are almost free from the spurious center-of-mass motion. However, for the lowest $K = 1$ dipole state in ¹⁵⁴Sm, we see a large difference between the two calculations. This implies that the full self-consistency is necessary to describe quantitatively the low-lying dipole states. The contamination of the spurious mode is smaller in the low-lying octupole excitations and in the GRs as shown in the lower panel of Fig. 1.

C. Giant resonances

Let us discuss properties of GRs. In order to quantify the excitation energy of the GR, two kinds of definition are utilized. The centroid energy E_c is frequently used in the experimental analysis, defined by

$$E_c = \frac{m_1}{m_0}, \quad (17)$$

where m_k is a k -th moment of the transition strength distribution in an energy interval of $[E_a, E_b]$ MeV.

$$m_k \equiv \int_{E_a}^{E_b} E^k S_\lambda^\tau(E) dE, \quad (18)$$

where $S_\lambda^\tau(E)$ is defined by Eq. (6) in the calculation. We take the upper and lower limits, $[E_a, E_b]$, same as those used in the experimental analysis.

Another definition of the excitation energy is denoted as E_x . This is extracted by fitting the strength distribution of the GR, $S_\lambda^\tau(E)$, by the Lorentz curve with two parameters, the peak energy E_x and the width Γ .

1. Positive-parity excitation

Figure 2 shows the strength distributions of IS monopole and quadrupole excitations in the Nd and Sm

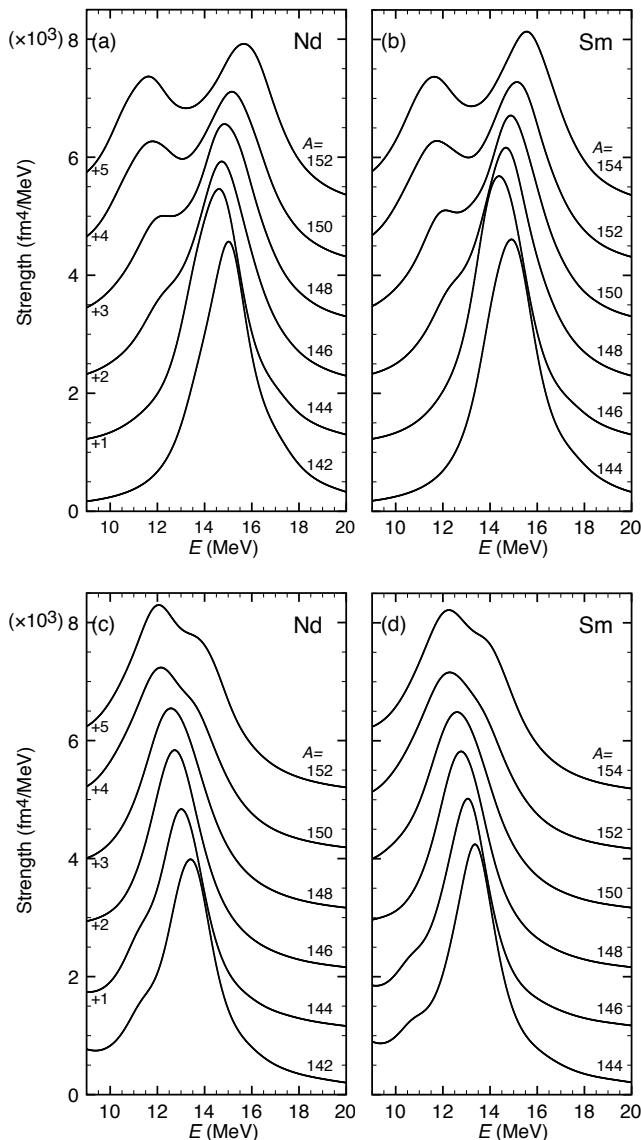


FIG. 2. The strength distributions (shifted) of ISGMR [(a), (b)] and ISGQR [(c), (d)] in Nd and Sm isotopes.

isotopes. We discuss first the giant quadrupole resonance (GQR). Both in the Nd and Sm isotopes, ISGQRs are located around 12–14 MeV. With increase in the mass number, the peak energy of the ISGQR becomes smaller. This is consistent with the experiment on the systematic observation of the ISGQR energy in the Sm isotopes [34, 36]. Figure 3 shows the centroid energy of the ISGQR in the Sm isotopes. Here we used the energy interval of [9,15] MeV. Open squares in Fig. 3 are obtained from the strength distribution in Ref. [34]. The present results well reproduce the experimental data. The calculated centroid energy is well fitted by the $65.6A^{-1/3}$ line, which agrees with the empirical behavior, $(64.0 \pm 1.7) \times A^{-1/3}$ [1]. Dependence on the

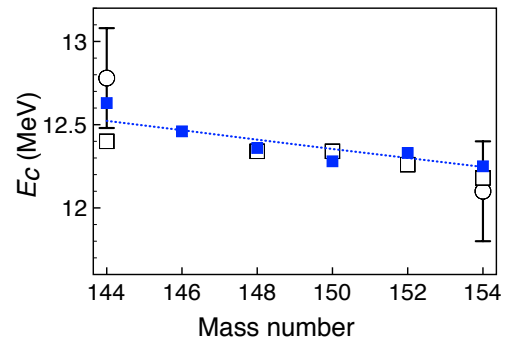


FIG. 3. (Color online) The centroid energies of the ISGQR in the Sm isotopes with a fitted line. The experimental data [35, 36] are denoted by open symbols.

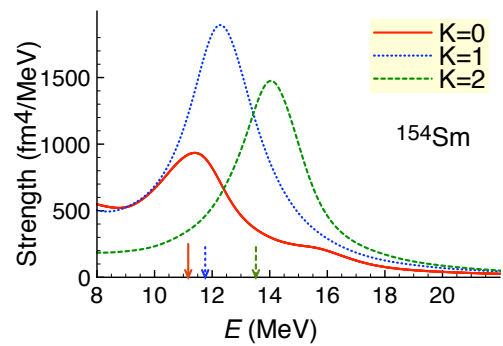


FIG. 4. (Color online) The IS quadrupole transition-strength distribution in ^{154}Sm for the $K^\pi = 0^+, 1^+, \text{ and } 2^+$ excitations. The eigenenergies obtained with use of the doubly-stretched P+Q model are denoted by the arrows, and the peak position of the GQR was adjusted to the experimental data [37].

choice of the Skyrme functional is discussed later.

The ISGQR in spherical nuclei was successfully described by the pairing-plus-quadrupole (P+Q) model. However, the same model failed to reproduce the observed data in deformed nuclei. This failure can be attributed to the violation of the nuclear self-consistency between the shapes of the potential and the density distributions. Making use of the quadrupole operator in doubly-stretched coordinates significantly improves the results [37]. It is due to the fact that the doubly-stretched quadrupole operator appropriately describes the quadrupole fluctuation about a deformed ground state [38]. In fact, the predicted deformation splitting of the ISGQR in ^{154}Sm is calculated to be about 2 MeV using the doubly-stretched P+Q model, whereas it is about 6 MeV using the ordinary P+Q model.

Figure 4 shows the IS quadrupole transition-strength distribution in ^{154}Sm for the $K^\pi = 0^+, 1^+$ and 2^+ excitations. The K splitting, $E_{K=2} - E_{K=0}$, for the ISGQR is 2.8 MeV in the present calculation. This is consistent

with the value obtained in the doubly-stretched P+Q model and the experimental observation [37]. This indicates that the present calculation based on the EDF naturally takes into account the nuclear self-consistency, which has to be introduced explicitly in the P+Q model where the higher-order terms are required additionally to satisfy the nuclear self-consistency [39]. Since the energy splitting associated with the deformation is comparable to the smearing parameter, the deformation splitting, which is clearly visible in the photoabsorption cross sections [16], does not appear in the ISGQR. Instead, we find a broadening of the width for the ISGQR associated with the development of the deformation (see the table in Appendix B).

Next, let us discuss the monopole excitation. In the spherical nuclei, we can see a sharp peak at around 15 MeV which is identified as the ISGMR. In ^{144}Sm , the peak energy and the width are $E_x = 14.8$ MeV and $\Gamma = 2.61$ MeV. This is compatible with the observed values of $E_x = 15.40 \pm 0.30$ and $\Gamma = 3.40 \pm 0.20$ MeV [36].

The ISGMR in deformed nuclei has a double-peak structure. The lower-energy peak ($8 < E < 13.5$ MeV) and the higher-energy peak ($13.5 < E < 19$ MeV) exhaust 31.4% and 60.6% of the IS monopole energy-weighted-sum rule (EWSR) value, $3.38 \times 10^5 \text{ fm}^4 \text{ MeV}$, in ^{154}Sm . The higher-energy peak of the IS monopole strength is identified as a primal ISGMR and the lower-energy peak is associated with the coupling to the $K^\pi = 0^+$ component of the ISGQR. The lower peak of the ISGMR around 11 MeV, is located at the peak position of the $K^\pi = 0^+$ component of the ISGQR shown in Fig. 4.

Figure 5(a) shows the peak energy of the ISGMR in the Sm isotopes. The calculation shows an excellent agreement with the experimental data both in spherical and deformed nuclei. As the deformation develops from ^{148}Sm , the higher-energy peak of the ISGMR slightly increases. In Fig. 5(b), the energy difference of the upper and lower peaks of the ISGMR is shown as a function of the deformation parameter of the ground state. The results are compared with the predictions by the fluid-dynamics model and the simple scaling model with the effective mass $m^*/m = 0.8$ and the Landau parameter $F_0 = -0.25$ [40]. The result of the fluid-dynamics model is consistent with our result, although it underestimates the excitation energy of the low-energy peak of ISGMR. The deformation dependence of the splitting energy is well reproduced. On the other hand, the simple scaling model significantly overestimates the ISGMR peak energy, which results in too large splitting of the peak energies.

Since the experimental studies for the detailed structure of the ISGMR in ^{154}Sm are available [36, 42], we are going to discuss here the properties of the calculated ISGMR in ^{154}Sm . Table II summarizes the parameters of the ISGMR in ^{154}Sm . The peak energy E_x and the width Γ in a deformed system are obtained by fitting the strength distribution with a sum of two Lorentz lines. The calculations are compared with inelastic α scatter-

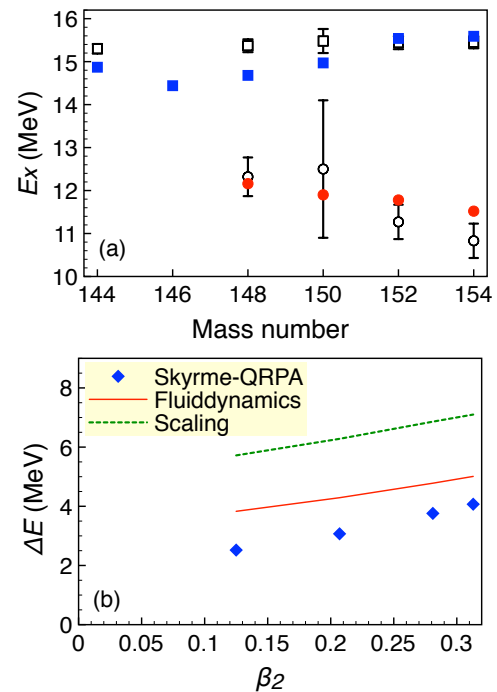


FIG. 5. (Color online) (a) The excitation energies of the ISGMR in the Sm isotopes. The experimental data [34] are denoted by open symbols with error bars. (b) The energy difference of the upper peak and the lower peak of the ISGMR in $^{148,150,152,154}\text{Sm}$ as a function of the deformation parameter β_2 . The lines are results of the fluid-dynamical and scaling models [40].

ing experiments at Texas A&M University [36] and at RCNP, Osaka University [42]. Results of the calculations employing the SLy4 [44] and SkP [19] functionals and other models [40, 43] are also shown. The same pairing energy functional, Eq. (3), is used in all the calculations.

The excitation energies are described best by the SkM* functional among three kinds of functionals. The ratio of the energy-weighted sum of the strengths for the upper peak to that for the lower peak varies from 1.6 (SLy4) to 3.2 (SkP), and the SkP gives better agreement with the experimental data. This implies that the coupling effect between the GMR and the GQR is weaker for the SkP functional than for the SkM* and SLy4 functionals. As discussed above, the coupling is determined by the quadrupole moment (deformation parameter) of the ground state. Indeed, the mass deformation parameter obtained in the present calculation is $\beta_2 = 0.29$ for SkP, while $\beta_2 = 0.31$ for SkM* and SLy4.

Figure 6 shows the strength distributions for the isovector (IV) monopole and quadrupole excitations. Although the experimental data for the IVGMR and IVGQR are unavailable in the mass region under investigation, the present calculation suggests the existence of these GR modes in the Nd and Sm isotopes. The energy of IVGQR is approximately fitted by 129.5 and

TABLE II. The parameters of the ISGMR in ^{154}Sm . Fitting the strength function $S_0^0(E)$ with $\gamma = 2$ MeV by a sum of two Lorentz lines, the peak energy E_x and the width Γ are extracted. The energy-weighted sum (EWS) of the transition strength is calculated in the energy range of [8,13.5] MeV and [13.5,19] MeV for the lower peak and upper peak of the ISGMR in the calculation using the SkM* functional. The energy range is slightly changed according to the shift of peak positions of the ISGMR in the calculations using the SLy4 and SkP functionals. The experimental values are taken from Refs. [36] and [42]. Results of other calculations employing different kinds of model in Refs. [40] and [43] and are also included.

	Lower peak			Upper peak			Ratio of EWS Upper/Lower
	E_x (MeV)	Γ (MeV)	EWS %	E_x (MeV)	Γ (MeV)	EWS %	
SkM*	11.5	3.75	31.4	15.6	2.73	60.6	1.9
SLy4	12.1	3.62	36.3	16.2	2.68	57.0	1.6
SkP	10.3	3.48	21.8	14.7	2.78	70.8	3.2
TAMU [36]	11.05 ± 0.05	3.2 ± 0.1	32 ± 2	15.17 ± 0.05	4.0 ± 0.1	80 ± 5	2.5 ± 0.2
RCNP [42]	11.0 ± 0.8	(5.1)	17.5 ± 5	15.6 ± 0.2	(3.9)	69 ± 5	3.9 ± 1.2
Fluidynamics [40]	10.1		21.5	15.6		76.3	3.5
Scaling [40]	11.0		16.6	18.1		83.4	5.0
Cranking [43]	10.4		21	15.9		79	3.8

$130.3 \times A^{-1/3}$ MeV for Nd and Sm isotopes, respectively. This is consistent with the experimental observations $\sim 130A^{-1/3}$ MeV in $A = 140 - 240$ nuclei [45]. The K -splitting of the IVGQR in deformed nuclei is invisible because the K -splitting is small.

A double-peak structure can be seen in deformed nuclei for the IVGMR as well as for the ISGMR. The lower peak around 20 MeV in the deformed nuclei emerges associated with the coupling to the $K^\pi = 0^+$ component of the IVGQR. The upper peak around 30 MeV may be identified as a primal IVGMR because the resonance peak appears in this energy region in the spherical nuclei. Similarly to the ISGMR, the upper peak of the IVGMR is upward-shifted with increasing the neutron number. This is due to the stronger coupling between the IVGMR and the IVGQR in nuclei with larger deformation. The energy difference between the upper and lower peaks of the IVGQR in ^{154}Sm approaches about 10 MeV, which is more than twice as large as the energy difference seen in the ISGMR.

2. Negative-parity excitation

Figure 7 shows the strength distributions of the IS compression dipole and octupole excitations. In the IS octupole-transition-strength distributions, we can see a high-energy octupole resonance (HEOR) at around 25 MeV. Furthermore, we find a broadening of the width associated with the deformation as observed in the experiment [46]. We show the centroid energy of the HEOR and the low-energy octupole resonance (LEOR) in the Sm isotopes in Fig. 8(b). The centroid energy of HEOR and LEOR is evaluated in the energy range of [17, 33] MeV and [3,10] MeV, respectively. The calculated energy of HEOR is best fitted to a $124.8 \times A^{-1/3}$ line, and agrees with the experimental observation [34]. However,

this excitation energy is significantly higher than the systematic value of $110 \pm 5 \times A^{-1/3}$ MeV [1].

Below 10 MeV, we find low-lying collective (discrete) states and the LEOR. The right panels of Fig. 9 show the low-energy part of the IS octupole transition-strengths in the Sm isotopes. We find that the low-lying collective $K = 2, 3$ states are overlapping with the LEOR in the well-deformed nuclei. The present calculation gives 6.5% and 24% of the IS octupole EWSR value in ^{154}Sm for the energy intervals 0 – 3 MeV and 0 – 7 MeV, respectively. This is compatible to the experimental value of 7% and 19% for the discrete states only and for the low-lying states including the discrete levels and the LEOR, respectively [47]. The early theoretical calculation employing the pairing plus octupole interaction model gives also an excellent agreement with the observed value by adjusting the interaction strengths [48].

The calculated octupole strength carries 51 – 53 % of the EWSR value in the HEOR energy region of 17 – 33 MeV. On the contrary, the experiment [34] has reported decrease of the strength in the same energy region from 75% to 30% of EWSR as increasing the mass number in the Sm isotopes. This inconsistency may be attributed to the uncertainty of the choice of the continuum in the experimental analysis and the strong overlap with the ISGDR [1].

We have the ISGDR at around 25 MeV corresponding to the $3\hbar\omega$ excitation, and this energy region is where the HEOR is located. We show the centroid energy of the ISGDR in the Sm isotopes in Fig. 8(a). The calculated energy is best fitted to the $130.7 \times A^{-1/3}$ line. The fitted energy of the ISGDR is slightly higher than that of the HEOR. The ISGDR in spherical nuclei is investigated in the framework of the HF-BCS + QRPA approach employing several Skyrme functionals [49]. The excitation energy obtained in Ref. [49] in ^{144}Sm is consistent with our result.

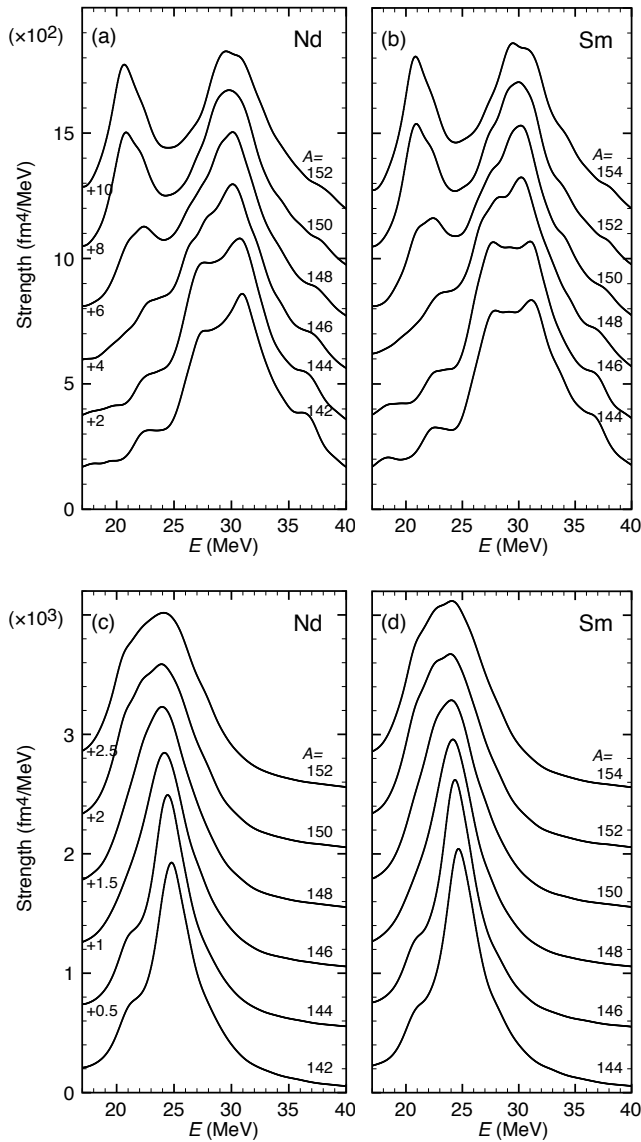


FIG. 6. The strength distributions (shifted) of IVGMR [(a), (b)] and IVGQR [(c), (d)] in Nd and Sm isotopes.

A deformation effect on the ISGDR can be seen in the increase of its width. This is due to the deformation splitting of the $K = 0$ and 1 components of the ISGDR similarly in the photoabsorption cross sections. Furthermore, the width becomes even larger due to the coupling to the $K = 0$ and 1 components of the HEOR. Figures 10(a) and (c) show the strength distributions of the IS dipole and octupole excitations in ^{154}Sm . The resonance structure at 26–28 MeV appears due to the deformation splitting of the primal ISGDR, and the structure at 20–23 MeV is due to the coupling to the $K = 0, 1$ components of the HEOR. Because of these two effects, the total strength distribution becomes very broad. When we fit the calculated strength distribution with a Lorentz

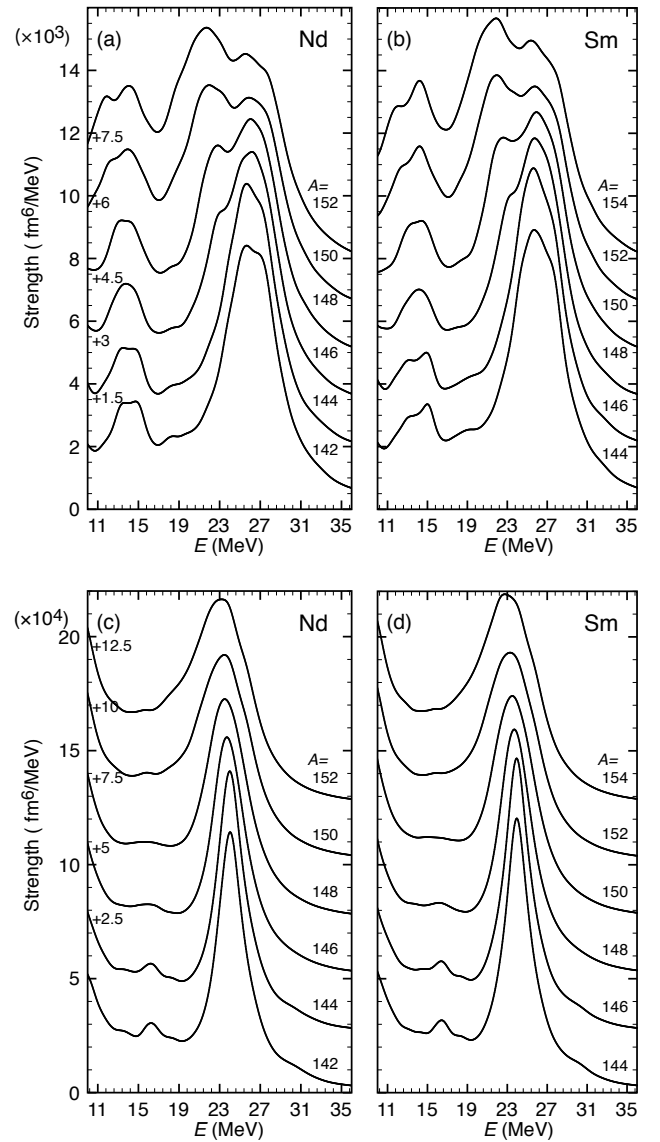


FIG. 7. Strength distributions (shifted) of ISGDR [(a), (b)] and ISGOR (HEOR) [(c), (d)] in Nd and Sm isotopes.

line in the energy region of [15, 35] MeV, we obtain the width $\Gamma = 13.4$ MeV. The large width is observed experimentally as 22.6 ± 4.2 MeV in Ref. [34], while the rather small width (11.8 ± 0.5 MeV) is reported in Ref. [36].

We furthermore find a low-energy (LE) ISGDR at about 14 MeV. We also find that the low-lying dipole states appear below 5 MeV with possession of large transition strengths in the deformed systems as shown in the left panels of Fig. 9. This is due to the coupling to the low-lying octupole modes of excitation.

The strength distribution in ^{154}Sm obtained by the (α, α') experiment in Ref. [36] shows a three-peak structure at around the excitation energy of 12 – 16 MeV, 20 – 24 MeV and 26 – 29 MeV. The data were compared

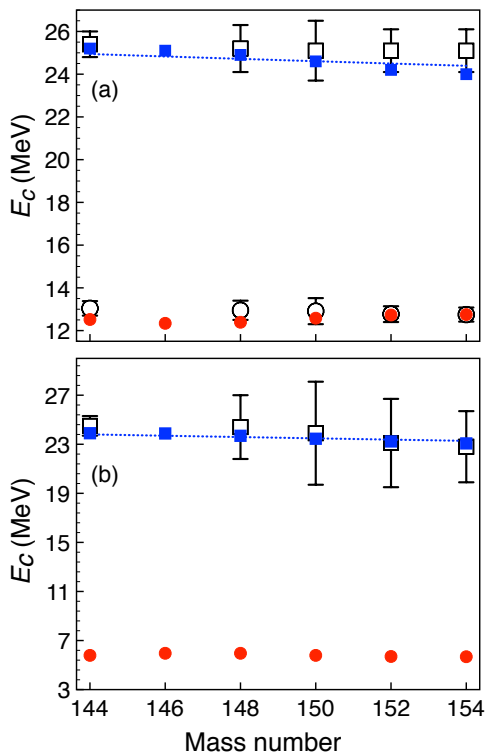


FIG. 8. (Color online) (a) The centroid energies of the low-energy and high-energy components of the ISGDR in the Sm isotopes. (b) The centroid energies of the HEOR and the LEOR in the Sm isotopes. The centroid energy of LEOR is evaluated in the energy range of $[E_a, E_b] = [3, 10]$ MeV. The dotted line is obtained by fitting the results with an $A^{-1/3}$ line. The experimental data [34] are denoted by open symbols with error bars.

with the fluidynamics results of Ref. [40], however, the mechanism for appearance of the second peak was unclear. According to the present calculation, it is suggested that the first peak corresponds to the low-energy ISGDR, the second peak is associated with the coupling to the $K = 0$ and 1 components of the HEOR, and the third peak is the primal ISGDR.

Figure 11 shows the strength distributions of IV dipole and octupole excitations. The IV giant octupole resonance (GOR) is seen above 30 MeV, and we find a bump structure at around 10 MeV corresponding to the IV-LEOR. The strength is rather smaller than that of the IV-HEOR. Noted that the strength of the IS-LEOR is compatible to that of the IS-HEOR.

In the deformed systems, we see an appearance of the shoulder structure at about 15 MeV. Figure 10 (b) and (d) presenting the IV dipole and octupole strength distributions in ^{154}Sm show that the shoulder structure is associated with the deformation splitting of the GDR and its coupling to the IV-LEOR.

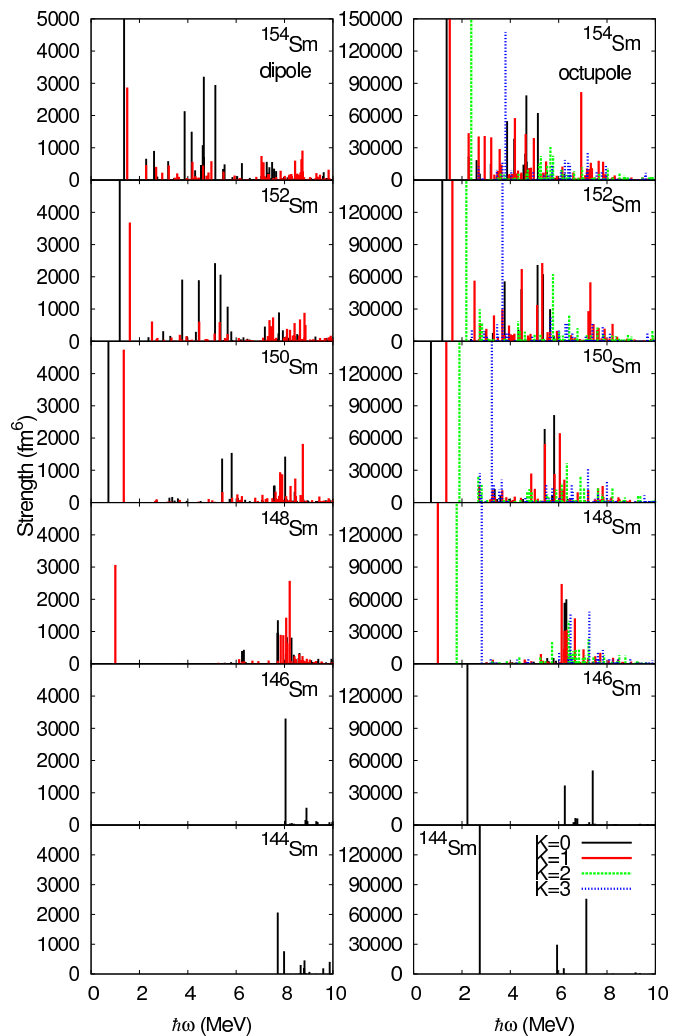


FIG. 9. (Color online) The low-energy IS dipole and octupole transition strengths in the Sm isotopes. The strengths with different K are all identical for the spherical nuclei.

3. Low-lying collective states

In this subsection, we are going to discuss the low-lying states. As shown in Fig. 9, we see an appearance of the collective mode for the IS dipole excitation below 2 MeV associated with an onset of deformation. This is due to the strong coupling to the collective octupole mode of excitation.

What has to be mentioned here is an absence of the collective $K = 0$ mode in ^{148}Sm . In the present calculation, we have two imaginary solutions in the $K^\pi = 0^-$ channel, one of which is associated with the spurious center-of-mass motion. In ^{150}Sm , we have the $K = 0$ mode at 0.72 MeV. The excitation energy of the collective $K = 0$ mode becomes higher when increasing the neutron number. Thus, we can consider that the second imaginary solution in ^{148}Sm indicates the instability against the axially-symmetric octupole deformation. In

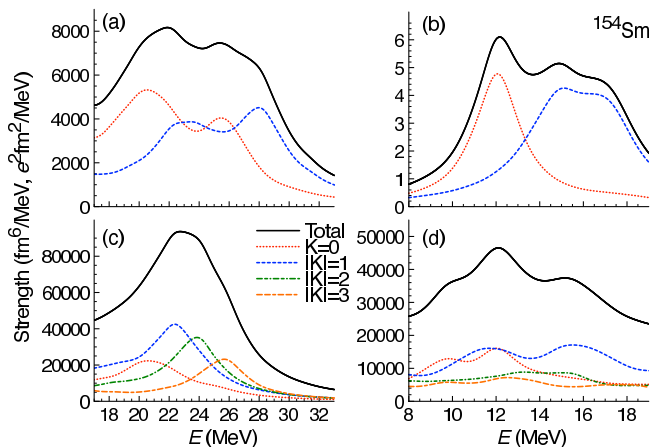


FIG. 10. (Color online) (a) The IS compression dipole strength distribution in the ISGDR energy region in ^{154}Sm . (b) The IV dipole strength distribution in the GDR energy region. (c) The IS octupole strength distribution. (d) The IV octupole strength distribution.

TABLE III. The excitation energies (in units of MeV) of the low-lying collective states in ^{154}Sm . Experimental data are taken from Ref. [50].

	$K^\pi = 0^+$	$K^\pi = 2^+$	$K^\pi = 0^-$	$K^\pi = 1^-$
SkM*	1.55	1.93	1.37	1.49
SLy4	1.46	1.81	1.25	1.66
SkP	0.95	0.92	1.44	1.64
Exp.	1.099	1.440	0.921	1.475

fact, the largest $B(E3; 0_1^+ \rightarrow 3_1^-)$ value is measured in ^{148}Sm among the even-even Sm isotopes [50].

Before going to the next subsection, we summarize the energy of the low-lying collective states in the spherical and the well-deformed Nd and Sm isotopes. Figure 12 shows the excitation energies of the lowest $K^\pi = 0^+, 2^+, 0^-$ and 1^- states. The available experimental data [50] are also shown. For the experimental values, we neglect the rotational correction, which is 30 keV at most in ^{154}Sm . Figure 12 shows that the observed isotopic dependence is well reproduced.

The excitation energies of the quadrupole-vibrational states agree with the experimental data within 0.5 – 1 MeV. This result is close to the one obtained in Ref. [51], where they obtained the γ -vibrational state at 2.5 MeV and at 2.3 MeV in ^{152}Nd and in ^{154}Sm , respectively despite the use of a different pairing functional from ours. Reproduction of the experimental values of the octupole-vibrational states in the deformed nuclei is extremely good.

Table III summarizes the excitation energy of the low-lying collective states in ^{154}Sm obtained by the QRPA calculations employing the different kinds of Skyrme functionals. All the Skyrme functionals under considera-

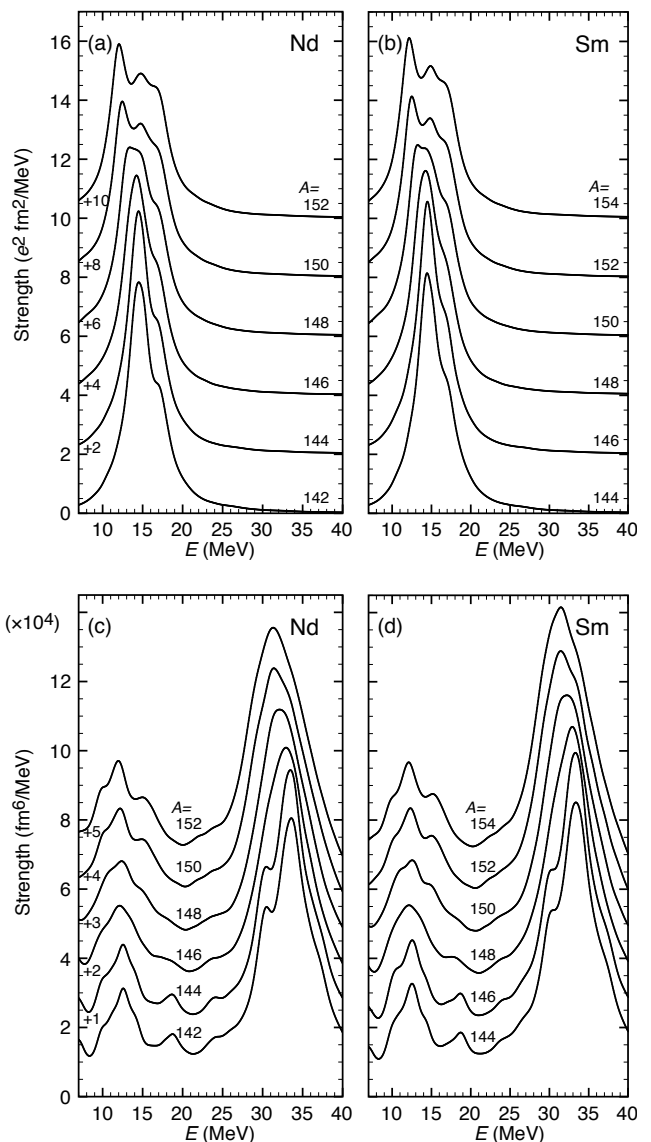


FIG. 11. The strength distributions (shifted) of IVGDR [(a), (b)] and IVGOR [(c), (d)] in Nd and Sm isotopes.

tion give a reasonable agreement with the measurements, and the quality is at the same level found in Ref. [30].

D. Incompressibility and effective mass in GRs

In this subsection, we investigate how the calculated properties of the GRs depend on the Skyrme EDFs with the different nuclear matter properties, effective mass and the incompressibility. We take ^{144}Sm and ^{154}Sm as examples of spherical and deformed nuclei, respectively. The experimental data for all the isoscalar multipole excitations are available for these isotopes. Nuclear matter and deformation properties for the functionals we employ are

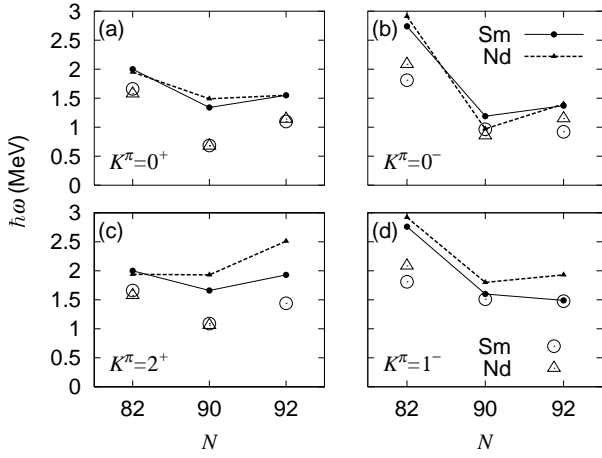


FIG. 12. The excitation energies of the lowest $K^\pi = 0^+, 2^+, 0^-$ and 1^- states in Nd and Sm isotopes. The experimental data for Nd and Sm isotopes [50] are denoted by open triangles and circles, respectively. The lines are drawn to guide the eyes.

TABLE IV. The nuclear matter and deformation properties for the Skyrme functionals under consideration. The table represents the isoscalar effective mass m_0^*/m , the nuclear-matter incompressibility K , and the deformation parameters β_2 in ^{154}Sm .

Forces	m_0^*/m	K (MeV)	β_2^ν	β_2^s
SkM*	0.79	216.7	0.30	0.33
SLy4	0.70	229.9	0.30	0.33
SkP	1.00	201.0	0.28	0.30

listed in Table IV.

As we discussed in Section III C 1, the experimental value for the peak energies of the ISGMR is fairly reproduced in the calculation for all the functionals under investigation. The excitation energies of the upper peak of the ISGMR in ^{154}Sm and the ISGMR in ^{144}Sm are shown in the upper-left panels of Fig. 13 as functions of the square root of the incompressibility. We can see a clear correlation between them. This result is consistent with the fact that the GMR energy is proportional to the square root of the incompressibility [52]. The excitation energy is given in the scaling model as

$$\omega_M^s = \sqrt{5(m/m_0^*)(1 + F_0)}\Omega = \sqrt{5K/3m\langle r^2 \rangle}, \quad (19)$$

where F_0 is the Landau-Migdal parameter and $\hbar\Omega \simeq 41A^{-1/3}$ (MeV) [40], and the excitation energy of the upper peak of the ISGMR in deformed systems is given in Eq. (3.10) of Ref. [40]. Note here that as we saw in Sec. III C 1 the scaling model overestimates the energy of the compressible modes, while it gives the qualitative understanding of GRs [40]. Since the SkP functional has a small incompressibility, the calculated excitation en-

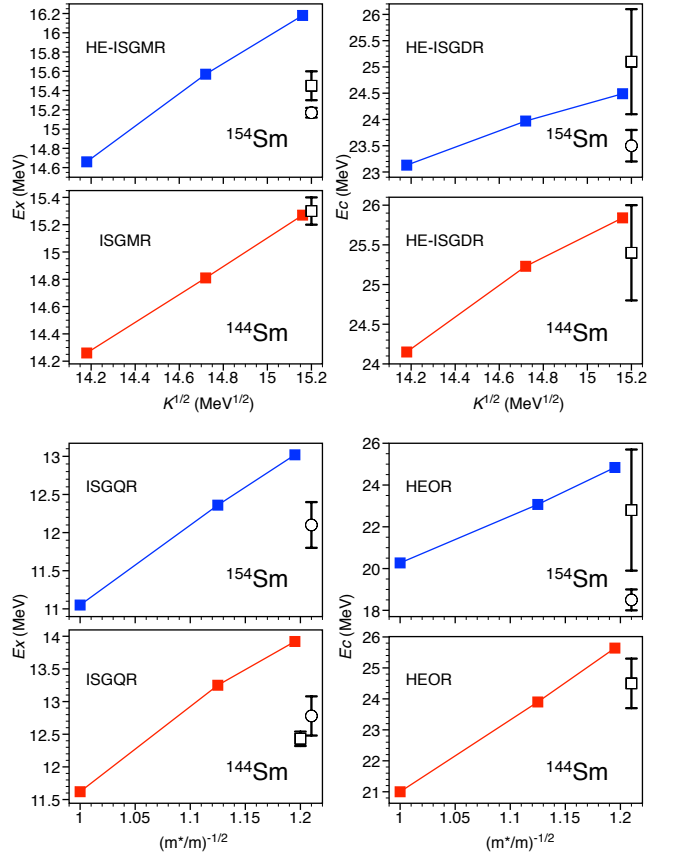


FIG. 13. (Color online) The peak energies of the ISGMR and ISGQR, and the centroid energy of the ISGDR and HEOR in ^{144}Sm and ^{154}Sm obtained by employing the Skyrme functionals giving the different nuclear-matter properties. The continuous lines are drawn to guide the eyes. Experimental data are shown by the open square [34] and the circle [36] with the error bars.

ergy of the ISGMR is lower than the experimental data and the results obtained by using the SkM* and SLy4 functionals.

For the GMR in ^{154}Sm , the SkM* functional gives the excitation energy which is very close to the observation [34]. However, in ^{144}Sm the SkM* underestimates the observation, and the SLy4 gives the reasonable energy. The experimental data reported in Refs. [36, 53] for the GMR centroid energy in ^{144}Sm are 15.39 ± 0.28 MeV and 15.40 ± 0.30 MeV. Therefore, the present calculation suggests that the nuclear-matter incompressibility is about $15.2^2 = 231$ MeV deduced from the comparison for ^{144}Sm and $14.6^2 = 213$ MeV for ^{154}Sm . As mentioned in Section III A, the pairing properties in ^{144}Sm and ^{154}Sm are quite different. Thus it would be interesting to investigate in detail the pairing effects on the GMR [54, 55], taking the deformation effect into account.

The upper-right panel of Fig. 13 shows the the centroid energy of the ISGDR. Here, we evaluate the centroid en-

ergy in the energy region of the second and the third peaks as done in the experimental analysis [34, 36] for ^{154}Sm . The excitation energy of the ISGDR is given in the scaling model as [40]

$$\omega_{\text{D}}^{\text{s}} = \sqrt{\frac{7}{3} \left[\frac{5K}{3m\langle r^2 \rangle} + \frac{8}{5} \left(\frac{m}{m_0^*} \right) \right]} \Omega. \quad (20)$$

It contains information not only of the incompressibility but of the effective mass. Note that the primal ISGDR in the deformed nuclei is the third peak as we discussed in the previous section.

In the left-lower and right-lower panels of Fig. 13, we show the peak energy of the ISGQR and the centroid energy of the HEOR as functions of the inverse of square root of the isoscalar effective mass $\sqrt{m_0^*/m}^{-1}$. We can see a linear correlation between them: The smaller the isoscalar effective mass, the higher the resonance energy. This is consistent with the results of the simple model. The excitation energy of the ISGQR and HEOR is given by the scaling model as [40]

$$\omega_{\text{Q}}^{\text{s}} = \sqrt{2(m/m_0^*)} \Omega, \quad (21)$$

$$\omega_{\text{O}}^{\text{s}} = \sqrt{(28/5)(m/m_0^*)} \Omega. \quad (22)$$

This feature is also consistent with the finding in the GQR energy obtained by the RPA calculations for spherical systems [56].

For the ISGQR, the effective mass m_0^*/m around $1.09^{-2} = 0.84$ gives the excitation energy which is compatible with the experimental results both in ^{144}Sm and in ^{154}Sm . For the HEOR in ^{144}Sm , slightly smaller effective mass around $1.16^{-2} = 0.74$ seems to be favored in comparison with the experimental observation [34]. In ^{154}Sm , it is hard to deduce the optimal value for the effective mass due to the large error in the experiment [34].

The excitation energies of the HEOR in ^{144}Sm and ^{154}Sm reported in Ref. [36] are 19.6 ± 0.5 MeV and 18.5 ± 0.5 MeV, respectively. The error is much smaller than that in the experiment at RCNP [34]. However, the excitation energy is small and it is outside of the energy region obtained by the three types of Skyrme functionals. This indicates that the effective mass is around $0.95^{-2} = 1.11$ or even larger. Since the strength distribution of the ISGDR in Ref. [36] looks similar to our results, the large discrepancy found in the HEOR is difficult to understand.

IV. SUMMARY

We have investigated the deformation effects on GRs in the rare-earth nuclei by employing the newly developed parallelized computer code for the QRPA based on the Skyrme EDF. We found a good scalability for the calculation of the matrix elements of the QRPA equation

by the use of a two-dimensional block cyclic distribution, which is suited for the ScaLAPACK.

The axial deformation in the ground state allows the GRs with the multipolarity $L = 0$ and 2 to mix in the $K^\pi = 0^+$ channel. Accordingly, we have obtained a double-peak structure of the ISGMR. The energy difference between the upper and lower peaks in the ISGMR and the fraction of the energy-weighted summed strength in the lower peak can be a sensitive measure of the ground-state quadrupole moment. We also predict a prominent double-peak structure of the IVGMR.

For the negative-parity excitations, the excitation modes with $L = 1$ and 3 can mix in the $K^\pi = 0^-$ and 1^- channels. This mixing leads to a large width for the ISGDR and the enhancement of the low-lying dipole-transition strengths associated with coupling to the collective octupole mode of excitation. In the IV channel, the excitation energies of GDR and LEOR are similar. In deformed nuclei, the coupling between these two modes creates a broadening of the IV-LEOR peak.

It should be emphasized here that the origin of the observed peak splitting in the IVGDR is different from that of the other GRs. The double-peak structure in the IVGDR is well-known to be due to a direct consequence of the nuclear deformation [2]. Namely, this is associated with different frequencies between $K = 0$ and $K = 1$ modes in the axially deformed system. The same kind of deformation splitting, according to the different K quantum numbers, also exists in the other GRs, however, its magnitude is much smaller than the IVGDR. Typically, the magnitude of the K -splitting is about 2 MeV. Therefore, with the smearing width of $\gamma = 2$ MeV in the present calculation, the peak splitting disappears. The double-peak structures in deformed nuclei for ISGMR, IVGMR, ISGDR, and IV-LEOR, observed in the present calculation are all associated with the coupling among GRs with different multipolarity.

Calculations using several commonly used Skyrme functionals in the nuclear EDF method all give a fairly good reproduction of the experimental data, not only for the GRs but also for the low-lying collective modes in the spherical and the well deformed nuclei. Comparison of the GR results with the experimental data obtained at RCNP [34] and TAMU [36] was performed in details for the spherical nucleus ^{144}Sm and the deformed ^{154}Sm . The experimental data for the ISGMR and the ISGDR indicates the incompressibility around 210 – 230 MeV. The excitation energy of the ISGQR is well reproduced with the effective mass $m_0^*/m \simeq 0.8 - 0.9$ both in ^{144}Sm and in ^{154}Sm . The experimental data for the HEOR are very different between the two experiments [34, 36]. A further experiments for HEOR are needed to confirm the value of the effective mass.

ACKNOWLEDGMENTS

Valuable discussions with G. Colò are acknowledged. The work is supported in part by Grant-in-Aid for Scientific Research (Nos. 21340073, 20105003 and 23740223) and by the Joint Research Program at Center for Computational Sciences, University of Tsukuba. The numerical calculations were performed on RIKEN Integrated Cluster of Clusters (RICC), T2K at University of Tsukuba and SR16000 at the Yukawa Institute of Theoretical Physics, Kyoto University.

Appendix A: QRPA matrix elements

Using the quasiparticle wave functions $\varphi_1(\mathbf{r}\sigma)$ and $\varphi_2(\mathbf{r}\sigma)$, the solutions of the coordinate-space HFB equation, the matrix elements appearing in the QRPA matrix are written as

$$\begin{aligned}
A_{\alpha\beta\gamma\delta} &= (E_\alpha + E_\beta)\delta_{\alpha\gamma}\delta_{\beta\delta} \\
&+ \sum_{\sigma_1, \sigma_2, \sigma'_1, \sigma'_2} \int d\mathbf{r}_1 d\mathbf{r}_2 d\mathbf{r}'_1 d\mathbf{r}'_2 \times \\
&\{ \varphi_{1,\alpha}(\mathbf{r}_1\bar{\sigma}_1)\varphi_{1,\beta}(\mathbf{r}_2\bar{\sigma}_2)\bar{v}_{pp}(12; 1'2')\varphi_{1,\gamma}^*(\mathbf{r}'_1\bar{\sigma}'_1)\varphi_{1,\delta}^*(\mathbf{r}'_2\bar{\sigma}'_2) \\
&+ \varphi_{2,\alpha}(\mathbf{r}_1\sigma_1)\varphi_{2,\beta}(\mathbf{r}_2\sigma_2)\bar{v}_{pp}(12; 1'2')\varphi_{2,\gamma}^*(\mathbf{r}'_1\sigma'_1)\varphi_{2,\delta}^*(\mathbf{r}'_2\sigma'_2) \\
&- \varphi_{1,\alpha}(\mathbf{r}_1\bar{\sigma}_1)\varphi_{2,\gamma}^*(\mathbf{r}_2\sigma_2)\bar{v}_{ph}(12; 1'2')\varphi_{2,\beta}(\mathbf{r}'_1\sigma'_1)\varphi_{1,\delta}^*(\mathbf{r}'_2\bar{\sigma}'_2) \\
&- \varphi_{1,\beta}(\mathbf{r}_1\bar{\sigma}_1)\varphi_{2,\delta}^*(\mathbf{r}_2\sigma_2)\bar{v}_{ph}(12; 1'2')\varphi_{2,\alpha}(\mathbf{r}'_1\sigma'_1)\varphi_{1,\gamma}^*(\mathbf{r}'_2\bar{\sigma}'_2) \\
&+ \varphi_{1,\alpha}(\mathbf{r}_1\bar{\sigma}_1)\varphi_{2,\delta}^*(\mathbf{r}_2\sigma_2)\bar{v}_{ph}(12; 1'2')\varphi_{2,\beta}(\mathbf{r}'_1\sigma'_1)\varphi_{1,\gamma}^*(\mathbf{r}'_2\bar{\sigma}'_2) \\
&+ \varphi_{1,\beta}(\mathbf{r}_1\bar{\sigma}_1)\varphi_{2,\gamma}^*(\mathbf{r}_2\sigma_2)\bar{v}_{ph}(12; 1'2')\varphi_{2,\alpha}(\mathbf{r}'_1\sigma'_1)\varphi_{1,\delta}^*(\mathbf{r}'_2\bar{\sigma}'_2) \}, \\
\end{aligned} \tag{A1}$$

$$\begin{aligned}
B_{\alpha\beta\gamma\delta} &= \sum_{\sigma_1, \sigma_2, \sigma'_1, \sigma'_2} \int d\mathbf{r}_1 d\mathbf{r}_2 d\mathbf{r}'_1 d\mathbf{r}'_2 \times \\
&\{ -\varphi_{1,\alpha}(\mathbf{r}_1\bar{\sigma}_1)\varphi_{1,\beta}(\mathbf{r}_2\bar{\sigma}_2)\bar{v}_{pp}(12; 1'2')\varphi_{2,\bar{\gamma}}(\mathbf{r}'_1\sigma'_1)\varphi_{2,\bar{\delta}}(\mathbf{r}'_2\sigma'_2) \\
&- \varphi_{2,\alpha}(\mathbf{r}_1\sigma_1)\varphi_{2,\beta}(\mathbf{r}_2\sigma_2)\bar{v}_{pp}(12; 1'2')\varphi_{1,\bar{\gamma}}(\mathbf{r}'_1\bar{\sigma}'_1)\varphi_{1,\bar{\delta}}(\mathbf{r}'_2\bar{\sigma}'_2) \\
&+ \varphi_{1,\alpha}(\mathbf{r}_1\bar{\sigma}_1)\varphi_{1,\bar{\gamma}}(\mathbf{r}_2\bar{\sigma}_2)\bar{v}_{ph}(12; 1'2')\varphi_{2,\beta}(\mathbf{r}'_1\sigma'_1)\varphi_{2,\bar{\delta}}(\mathbf{r}'_2\sigma'_2) \\
&+ \varphi_{1,\beta}(\mathbf{r}_1\bar{\sigma}_1)\varphi_{1,\bar{\delta}}(\mathbf{r}_2\bar{\sigma}_2)\bar{v}_{ph}(12; 1'2')\varphi_{2,\alpha}(\mathbf{r}'_1\sigma'_1)\varphi_{2,\bar{\gamma}}(\mathbf{r}'_2\sigma'_2) \\
&- \varphi_{1,\alpha}(\mathbf{r}_1\bar{\sigma}_1)\varphi_{1,\bar{\delta}}(\mathbf{r}_2\bar{\sigma}_2)\bar{v}_{ph}(12; 1'2')\varphi_{2,\beta}(\mathbf{r}'_1\sigma'_1)\varphi_{2,\bar{\gamma}}(\mathbf{r}'_2\sigma'_2) \\
&- \varphi_{1,\beta}(\mathbf{r}_1\bar{\sigma}_1)\varphi_{1,\bar{\gamma}}(\mathbf{r}_2\bar{\sigma}_2)\bar{v}_{ph}(12; 1'2')\varphi_{2,\alpha}(\mathbf{r}'_1\sigma'_1)\varphi_{2,\bar{\delta}}(\mathbf{r}'_2\sigma'_2) \}. \\
\end{aligned} \tag{A2}$$

Here, the time-reversed state is defined as

$$\varphi_{\bar{i}}(\mathbf{r}\sigma) = -2\sigma\varphi_i^*(\mathbf{r} - \sigma). \tag{A3}$$

If one assumes that the effective pairing interaction is local, \bar{v}_{pp} is written as

$$\begin{aligned}
\bar{v}_{pp}(12; 1'2') &= V_{pp}(\mathbf{r}_1\sigma_1\tau_1, \mathbf{r}_2\sigma_2\tau_2) \times \\
&\delta(\mathbf{r}'_1 - \mathbf{r}_1)\delta_{\sigma'_1, \sigma_1}\delta_{\tau'_1, \tau_1}\delta(\mathbf{r}'_2 - \mathbf{r}_2)\delta_{\sigma'_2, \sigma_2}\delta_{\tau'_2, \tau_2}, \\
\end{aligned} \tag{A4}$$

and for V_{pp} we use the form

$$\begin{aligned}
V_{pp}(\mathbf{r}_1\sigma_1\tau_1, \mathbf{r}_2\sigma_2\tau_2) &= V_0 g_q[\varrho(\mathbf{r}_1), \varrho_1(\mathbf{r}_1)] \times \\
&\delta(\mathbf{r}_1 - \mathbf{r}_2)\delta_{\sigma_1, -\sigma_2}\delta_{\tau_1, \tau_2}. \\
\end{aligned} \tag{A5}$$

in the present paper.

Similarly, the effective interaction for the p-h channel reads

$$\begin{aligned}
\bar{v}_{ph}(12; 1'2') &= V_{ph}(\mathbf{r}_1\sigma_1\tau_1, \mathbf{r}_2\sigma_2\tau_2) \times \\
&\delta(\mathbf{r}'_1 - \mathbf{r}_1)\delta_{\sigma'_1, \sigma_1}\delta_{\tau'_1, \tau_1}\delta(\mathbf{r}'_2 - \mathbf{r}_2)\delta_{\sigma'_2, \sigma_2}\delta_{\tau'_2, \tau_2}, \\
\end{aligned} \tag{A6}$$

and we take the form

$$\begin{aligned}
V_{ph}(\mathbf{r}_1\sigma_1\tau_1, \mathbf{r}_2\sigma_2\tau_2) &= \\
&(a_0 + a'_0\boldsymbol{\tau}_1 \cdot \boldsymbol{\tau}_2 + (b_0 + b'_0\boldsymbol{\tau}_1 \cdot \boldsymbol{\tau}_2)\boldsymbol{\sigma}_1 \cdot \boldsymbol{\sigma}_2)\delta(\mathbf{r}_1 - \mathbf{r}_2) \\
&+ (a_1 + a'_1\boldsymbol{\tau}_1 \cdot \boldsymbol{\tau}_2 + (b_1 + b'_1\boldsymbol{\tau}_1 \cdot \boldsymbol{\tau}_2)\boldsymbol{\sigma}_1 \cdot \boldsymbol{\sigma}_2) \\
&\times (\mathbf{k}^{\dagger 2}\delta(\mathbf{r}_1 - \mathbf{r}_2) + \delta(\mathbf{r}_1 - \mathbf{r}_2)\mathbf{k}^2) \\
&+ (a_2 + a'_2\boldsymbol{\tau}_1 \cdot \boldsymbol{\tau}_2 + (b_2 + b'_2\boldsymbol{\tau}_1 \cdot \boldsymbol{\tau}_2)\boldsymbol{\sigma}_1 \cdot \boldsymbol{\sigma}_2) \\
&\times (\mathbf{k}^\dagger \cdot \delta(\mathbf{r}_1 - \mathbf{r}_2)\mathbf{k}) \\
&+ (a_4 + a'_4\boldsymbol{\tau}_1 \cdot \boldsymbol{\tau}_2)(\boldsymbol{\sigma}_1 + \boldsymbol{\sigma}_2) \cdot \mathbf{k}^\dagger \times \delta(\mathbf{r}_1 - \mathbf{r}_2)\mathbf{k} \\
\end{aligned} \tag{A7}$$

with the standard notations of \mathbf{k} and \mathbf{k}^\dagger . The coefficients in Eq. (A7) are given in Ref. [23]. The coefficients a_0, a'_0, b_0 and b'_0 are density dependent and include the rearrangement terms. In the present paper, we have an additional contribution to these terms coming from the pairing EDF (3). They are

$$\begin{cases} -\frac{V_0}{2} \frac{\eta_2}{\varrho_0^2} [\tilde{\varrho}_\nu^2(\mathbf{r}) + \tilde{\varrho}_\pi^2(\mathbf{r})] & \text{(for } \nu - \nu, \pi - \pi) \\ \frac{V_0}{2} \frac{\eta_2}{\varrho_0^2} [\tilde{\varrho}_\nu^2(\mathbf{r}) + \tilde{\varrho}_\pi^2(\mathbf{r})] & \text{(for } \nu - \pi). \end{cases} \tag{A8}$$

Appendix B: Parameters of the giant resonances

We summarize here the peak energy and the width of the GRs obtained by the calculations with the SkM* functional.

[1] M. N. Harakeh and A. van der Woude, *Giant Resonances: Fundamental High-Energy Modes of Nuclear Ex-*

citation (Oxford, 2001).

- [2] A. Bohr and B. R. Mottelson, *Nuclear Structure*, vol. II (Benjamin, 1975; World Scientific, 1998).
- [3] P. Carlos, H. Beil, R. Bergère, A. Leprêtre, and A. Veyssièrè, Nucl. Phys. **A172**, 437 (1971).
- [4] P. Carlos, H. Beil, R. Bergère, A. Leprêtre, A. De Miniac, and A. Veyssièrè, Nucl. Phys. **A225**, 171 (1974).
- [5] P. Ring and P. Schuck, *The Nuclear Many-Body Problem* (Springer, 1980).
- [6] M. Bender, P.-H. Heenen, and P.-G. Reinhard, Rev. Mod. Phys. **75** (2003) 121.
- [7] S. Péru and H. Goutte, Phys. Rev. C **77**, 044313 (2008).
- [8] V. O. Nesterenko, W. Kleinig, J. Kvasil, P. Vesely, P.-G. Reinhard, and D. S. Dolci, Phys. Rev. C **74**, 064306 (2006).
- [9] D. Pena Arteaga, E. Khan, and P. Ring, Phys. Rev. C **79**, 034311 (2009).
- [10] K. Yoshida and N. V. Giai, Phys. Rev. C **78**, 064316 (2008).
- [11] K. Yoshida, Eur. Phys. J. A. **42**, 583 (2009).
- [12] C. Losa, A. Pastore, T. Døssing, E. Vigezzi, R. A. Broglia, Phys. Rev. C **81**, 064307 (2010).
- [13] T. Nakatsukasa, T. Inakura, and K. Yabana, Phys. Rev. C **76**, 024318 (2007).
- [14] P. Avogadro and T. Nakatsukasa, Phys. Rev. C **84**, 014314 (2011).
- [15] M. Stoitsov, M. Kortelainen, T. Nakatsukasa, C. Losa, and W. Nazarewicz, Phys. Rev. C **84**, 041305R (2011).
- [16] K. Yoshida and T. Nakatsukasa, Phys. Rev. C **83**, 021304R (2011).
- [17] K. Yoshida, Phys. Rev. C **82**, 034324 (2010).
- [18] A. Bulgac, Preprint No. FT-194-1980, Institute of Atomic Physics, Bucharest, 1980. [arXiv:nucl-th/9907088]
- [19] J. Dobaczewski, H. Flocard, and J. Treiner, Nucl. Phys. **A422**, 103 (1984).
- [20] J. Bartel, P. Quentin, M. Brack, C. Guet, and H.-B. Håkansson, Nucl. Phys. **A386**, 79 (1982).
- [21] M. Yamagami, Y. R. Shimizu, and T. Nakatsukasa, Phys. Rev. C **80**, 064301 (2009).
- [22] D. J. Rowe, *Nuclear Collective Motion* (Methuen and Co. Ltd., 1970).
- [23] J. Terasaki, J. Engel, M. Bender, J. Dobaczewski, W. Nazarewicz and M. Stoitsov, Phys. Rev. C **71**, 034310 (2005).
- [24] Tapas Sil, S. Shlomo, B.K. Agrawal, and P. G. Reinhard, Phys. Rev. C **73**, 034316 (2006).
- [25] S. Ebata, T. Nakatsukasa, T. Inakura, K. Yoshida, Y. Hashimoto, and K. Yabana, Phys. Rev. C **82**, 034306 (2010).
- [26] T. Nakatsukasa, P. Avogadro, S. Ebata, T. Inakura and K. Yoshida, Acta Phys. Polon. B **42**, 609 (2011).
- [27] A. Baran, A. Bulgac, M. M. Forbes, G. Hagen, W. Nazarewicz, N. Schunck, and M. V. Stoitsov, Phys. Rev. C **78**, 014318 (2008).
- [28] N. Ullah and D. J. Rowe, Nucl. Phys. A **163**, 257 (1971).
- [29] <http://www.netlib.org/scalapack/>
- [30] J. Terasaki and J. Engel, Phys. Rev. C **82**, (2010) 034326.
- [31] G. F. Bertsch, C. A. Bertulani, W. Nazarewicz, N. Schunck, and M. V. Stoitsov, Phys. Rev. C **79**, 034306 (2009).
- [32] N. Van Giai and H. Sagawa, Nucl. Phys. **A371**, 1 (1981).
- [33] K. Yoshida, Phys. Rev. C **80**, 044324 (2009).
- [34] M. Itoh *et al.*, Phys. Rev. C **68**, 064602 (2003).
- [35] M. Itoh, private communications.
- [36] D. H. Youngblood, Y. -W. Lui, H. L. Clark, B. John, Y. Tokimoto, and X. Chen, Phys. Rev. C **69**, 034315 (2004).
- [37] T. Kishimoto, J. M. Moss, D. H. Youngblood, J. D. Bronson, C. M. Rozsa, D. R. Brown, and A. D. Bacher, Phys. Rev. Lett. **35**, 552 (1975).
- [38] H. Sakamoto and T. Kishimoto, Nucl. Phys. **A501**, 205 (1989).
- [39] H. Sakamoto and T. Kishimoto, Nucl. Phys. **A501**, 242 (1989).
- [40] S. Nishizaki and K. Andō, Prog. Theor. Phys. **73**, 889 (1985).
- [41] D. H. Youngblood, P. Bogucki, J. D. Bronson, U. Garg, Y. -W. Lui, and C. M. Rozsa, Phys. Rev. C **23**, 1997 (1981).
- [42] M. Itoh *et al.*, Phys. Lett. **B549**, 58 (2002).
- [43] Y. Abgrall, B. Morand, E. Caurier, and B. Grammaticos, Nucl. Phys. **A346**, 431 (1980).
- [44] E. Chabanat, P. Bonche, P. Haensel, J. Meyer, and R. Schaeffer, Nucl. Phys. **A635**, 231 (1998).
- [45] S. S. Henshaw, M. W. Ahmed, G. Feldman, A. M. Nathan, and H. R. Weller, Phys. Rev. Lett. **107**, 222501 (2011).
- [46] H. P. Morsch *et al.*, Phys. Lett. **119B**, 311 (1982).
- [47] J. M. Moss, D. H. Youngblood, C. M. Rozsa, D. R. Brown, and J. D. Bronson, Phys. Rev. Lett. **37**, 816 (1976).
- [48] L. A. Malov, V. O. Nesterenko, and V. G. Soloviev, J. Phys. G: Nucl. Phys. **3**, L219 (1977).
- [49] G. Colò, N. Van Giai, P. F. Bortignon, M. R. Quaglia, Phys. Lett. **B485**, 362 (2000).
- [50] <http://www.nndc.bnl.gov/ensdf/>
- [51] J. Terasaki and J. Engel, Phys. Rev. C **84**, 014332 (2011).
- [52] J. P. Blaizot, Phys. Rep. **64**, 171 (1980).
- [53] D. H. Youngblood, H. L. Clark, and Y.-W. Lui, Phys. Rev. Lett. **82**, 691 (1999).
- [54] J. Li, G. Colò, and J. Meng, Phys. Rev. C **78**, 064304 (2008).
- [55] E. Khan, J. Margueron, G. Colò, K. Hagino, and H. Sagawa, Phys. Rev. C **82**, 024322 (2010).
- [56] P.-G. Reinhard, Nucl. Phys. **A649**, 305c (1999).

TABLE V. The parameters of the ISGMR and IVGMR.

	ISGMR				IVGMR			
	E_x (MeV)	Γ (MeV)	E_x (MeV)	Γ (MeV)	E_x (MeV)	Γ (MeV)	E_x (MeV)	Γ (MeV)
¹⁴² Nd			15.0	2.67			30.0	10.7
¹⁴⁴ Nd			14.5	2.79			29.6	10.2
¹⁴⁶ Nd	12.1	2.37	14.8	3.05	21.9	7.47	29.7	9.68
¹⁴⁸ Nd	11.9	2.83	15.0	3.05	21.7	4.54	29.8	9.39
¹⁵⁰ Nd	11.8	3.22	15.6	3.15	21.1	3.92	30.2	9.81
¹⁵² Nd	11.5	3.40	15.7	3.20	20.7	3.91	30.3	9.76
¹⁴⁴ Sm			14.9	2.62			29.9	10.9
¹⁴⁶ Sm			14.4	2.68			29.4	10.4
¹⁴⁸ Sm	12.2	2.07	14.7	2.97	21.4	6.28	29.5	10.0
¹⁵⁰ Sm	11.9	2.79	15.0	2.97	21.6	4.27	29.8	9.52
¹⁵² Sm	11.8	3.20	15.5	3.04	21.2	3.79	30.2	9.90
¹⁵⁴ Sm	11.5	3.39	15.6	3.12	20.9	3.77	30.3	9.80

TABLE VI. The parameters of the ISGDR and IVGDR.

	LE-ISGDR		ISGDR				IVGDR			
	E_x (MeV)	Γ (MeV)	E_x (MeV)	Γ (MeV)	E_x (MeV)	Γ (MeV)	E_x (MeV)	Γ (MeV)	E_x (MeV)	Γ (MeV)
¹⁴² Nd	14.2	7.62	26.0	6.32			14.8	4.40		
¹⁴⁴ Nd	13.9	8.25	25.9	6.33			14.8	4.34		
¹⁴⁶ Nd	13.8	8.90	23.4	7.49	26.7	5.15	14.1	3.65	17.0	3.20
¹⁴⁸ Nd	13.8	9.26	22.3	5.78	26.7	5.71	13.5	3.58	16.5	4.73
¹⁵⁰ Nd	13.7	11.3	21.7	7.62	27.1	5.74	12.4	2.56	15.7	5.65
¹⁵² Nd	13.6	14.1	21.1	9.26	27.2	6.63	12.0	2.56	15.7	5.69
¹⁴⁴ Sm	14.3	9.52	25.9	6.20			14.8	4.38		
¹⁴⁶ Sm	13.9	10.5	25.8	6.21			14.8	4.31		
¹⁴⁸ Sm	14.0	10.3	23.6	7.59	26.7	4.95	14.1	3.58	16.9	3.45
¹⁵⁰ Sm	14.0	9.77	22.2	5.69	26.6	5.87	13.3	3.30	16.0	4.96
¹⁵² Sm	14.0	10.8	21.4	6.44	26.8	7.87	12.4	2.46	15.7	5.68
¹⁵⁴ Sm	14.0	12.6	21.0	8.21	26.9	7.44	12.1	2.51	15.7	5.70

TABLE VII. The parameters of the ISGQR and IVGQR.

	ISGQR		IVGQR	
	E_x (MeV)	Γ (MeV)	E_x (MeV)	Γ (MeV)
¹⁴² Nd	13.3	2.89	24.8	5.20
¹⁴⁴ Nd	12.9	2.93	24.5	5.12
¹⁴⁶ Nd	12.7	3.01	24.0	5.71
¹⁴⁸ Nd	12.6	3.51	23.5	6.69
¹⁵⁰ Nd	12.7	4.71	23.7	8.42
¹⁵² Nd	12.5	5.23	23.5	9.11
¹⁴⁴ Sm	13.3	2.73	24.8	4.96
¹⁴⁶ Sm	12.9	2.77	24.5	4.91
¹⁴⁸ Sm	12.7	3.02	24.2	5.59
¹⁵⁰ Sm	12.6	3.63	23.8	6.66
¹⁵² Sm	12.7	4.71	23.7	8.06
¹⁵⁴ Sm	12.6	5.14	23.5	8.64

TABLE VIII. The parameters of the HEOR and IVGOR.

	HEOR		IV-LEOR				IV-HEOR	
	E_x (MeV)	Γ (MeV)	E_x (MeV)	Γ (MeV)	E_x (MeV)	Γ (MeV)	E_x (MeV)	Γ (MeV)
¹⁴² Nd	24.1	3.65	12.5	6.97			33.3	8.02
¹⁴⁴ Nd	24.0	3.73	12.4	7.68			33.1	7.85
¹⁴⁶ Nd	23.8	4.44	12.2	9.94			32.8	8.01
¹⁴⁸ Nd	23.5	5.31	11.8	8.26	16.4	4.76	32.4	8.38
¹⁵⁰ Nd	23.2	6.47	11.5	6.29	16.0	4.86	32.0	9.28
¹⁵² Nd	22.9	6.84	11.5	6.01	16.0	4.55	31.7	9.73
¹⁴⁴ Sm	24.0	3.70	12.4	6.83			33.2	7.78
¹⁴⁶ Sm	24.0	3.66	12.3	7.48			33.1	7.61
¹⁴⁸ Sm	23.8	4.41	12.2	9.63			32.7	7.83
¹⁵⁰ Sm	23.4	5.51	11.9	8.28	16.2	4.56	32.3	8.32
¹⁵² Sm	23.1	6.84	11.8	6.36	16.1	4.49	32.0	9.00
¹⁵⁴ Sm	22.9	6.74	11.7	6.10	16.1	4.21	31.7	9.34